

Unstructured Versus Structured GLRT for Multipolarization SAR Change Detection

Vincenzo Carotenuto, *Student Member, IEEE*, Antonio De Maio, *Fellow, IEEE*, Carmine Clemente, *Member, IEEE*, and John Soraghan, *Senior Member, IEEE*

Abstract—Coherent multipolarization synthetic aperture radar (SAR) change detection exploiting data collected from N multiple polarimetric channels is addressed in this letter. The problem is formulated as a binary hypothesis testing problem, and a special block-diagonal structure for the polarimetric covariance matrix is forced to design a detector based on the generalized likelihood ratio test (GLRT) criterion. It is shown that the structured decision rule ensures the constant false alarm rate property with respect to the unknown disturbance covariance. Results on both simulated and real high-resolution SAR data show the effectiveness of the considered decision rule and its superiority against the traditional unstructured GLRT in some scenarios of practical interest.

Index Terms—Change detection, multipolarization, structured generalized likelihood ratio test (GLRT).

I. INTRODUCTION

CHANGE detection remains one of the most demanding radar imaging challenges. Starting from a pair of coregistered temporally spaced synthetic aperture radar (SAR) images representing an area of interest, change detection represents the capability to identify changes occurring during the time between two acquisitions [1], [2]. Incoherent change detection is when the decision is performed exploiting only the intensity information of the image pair, whereas if both amplitude and phase of the reference and test images are used, the technique assumes the name of coherent change detection. In [3] and [4], the multipolarization signal model for the SAR change detection problem was laid down. The detection problem was formulated as a binary hypothesis test, and a decision rule based on the generalized likelihood ratio test (GLRT) was developed. Moreover, a performance analysis [3] of the GLRT was given in the form of receiver operating characteristics (ROC), namely, detection probability (P_d) versus false alarm probability (P_{fa}), quantifying the benefits of the multipolarization information in SAR change detection. More recently, in [5], the generalized Kittler and Illingworth thresholding algorithm based on the

Manuscript received November 21, 2014; revised January 14, 2015 and February 24, 2015; accepted March 25, 2015. Date of publication April 27, 2015; date of current version June 15, 2015. This work was supported in part by the Engineering and Physical Sciences Research Council Grant EP/K014307/1, the MOD University Defence Research Collaboration in Signal Processing and in part by the University of Naples “Federico II.”

V. Carotenuto and A. De Maio are with the Università degli Studi di Napoli “Federico II,” DIETI, 80125 Napoli, Italy (e-mail: vincenzo.carotenuto@unina.it; ademaio@unina.it).

C. Clemente and J. Soraghan are with the University of Strathclyde, Centre for Excellence in Signal and Image Processing, Department of Electronic and Electrical Engineering, G1 1XW Glasgow, U.K. (e-mail: carmine.clemente@strath.ac.uk; j.soraghan@strath.ac.uk).

Color versions of one or more of the figures in this paper are available online at <http://ieeexplore.ieee.org>.

Digital Object Identifier 10.1109/LGRS.2015.2418575

generalized Gaussian model has been applied to detect threshold values to identify changes, while in [6], a GLRT detector using both noisy and denoised data was used. In [7], a new and systematic framework for change detection based on the theory of invariance in hypothesis testing problems was developed for the multipolarimetric coherent change detection problem.

The aim of this letter is to exploit the block-diagonal structure for the polarimetric covariance matrix introduced in [8] and to devise a decision rule based on the GLRT criterion directly exploiting the I/Q components of the received multivariate complex Gaussian observations. This issue represents the main technical contribution of the present study. Furthermore, the considered detector ensures the constant false alarm rate (CFAR) property with respect to the unknown polarimetric covariance provided that it complies with the design structure. The benchmark clairvoyant optimum detector and the GLRT derived in [3] (without the exploitation of the special covariance structure forced by polarization diversity) are used as a benchmark at the analysis stage to assess the performance of the structured GLRT. The analysis, conducted both on simulated and real high-resolution SAR data, shows the effectiveness of the structured GLRT and its superiority over the classic unstructured GLRT in some scenarios of practical interest.

The remainder of this letter is organized as follows. The multipolarization SAR change detection problem is formulated, and the GLRT proposed in [3] is reported in Section II. In Section III, the derivation of the structured GLRT is introduced, while in Section IV, the performance is assessed for both simulated and real multipolarization SAR images. Finally, in Section V, the conclusion is provided.

A. Notation

We adopt the notation of using boldface for vectors and matrices. The conjugate transpose operator is denoted by the symbol $(\cdot)^\dagger$, while $\text{tr}(\cdot)$ and $\det(\cdot)$ are, respectively, the trace and the determinant of the square matrix argument. Finally, $\mathbf{0}$ denotes the matrix with zero entries (its size is determined from the context), while \mathcal{H}_N^{++} denotes the set of $N \times N$ Hermitian positive definite matrices.

II. PROBLEM FORMULATION

A multipolarization SAR sensor measures for each pixel of the image under test $N = 3$ complex returns, collected from different polarimetric channels (HH, VV, and HV). The N returns from the same pixel are stacked in the specific order HH, VV, and HV to form the vector $\mathbf{X}(l, m)$, where $l = 1, \dots, L$ and $m = 1, \dots, M$ (L and M represent the vertical and horizontal sizes

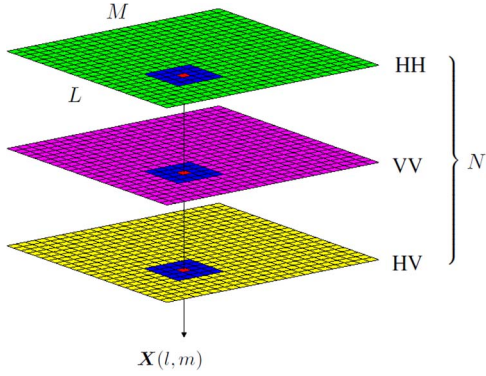


Fig. 1. Construction of the datacube.

of the image, respectively). Therefore, the sensor provides a 3-D data stack \mathbf{X} of size $M \times L \times N$, which is referred to in the following as a datacube and is illustrated in Fig. 1.

For SAR change detection applications, we assume that two datacubes \mathbf{X} (reference data) and \mathbf{Y} (test data) of the same geographic area are available. Furthermore, we suppose that they were collected from two different sensor passes and are accurately pixel aligned (coregistered).¹ We focus on the problem of detecting the presence of possible changes in a rectangular neighborhood \mathcal{A} , with size $K = W_1 \times W_2 \geq N$, of a given pixel. To this end, we denote with \mathbf{R}_X (\mathbf{R}_Y) the matrix whose columns are the vectors of the polarimetric returns from the pixels of \mathbf{X} (\mathbf{Y}) which fall in region \mathcal{A} and $\mathbf{S}_X = \mathbf{R}_X \mathbf{R}_X^\dagger$ ($\mathbf{S}_Y = \mathbf{R}_Y \mathbf{R}_Y^\dagger$).

The matrices \mathbf{R}_X and \mathbf{R}_Y are modeled as statistically independent random matrices. Moreover, the columns of \mathbf{R}_X (\mathbf{R}_Y) are assumed statistically independent and identically distributed random vectors drawn from a complex circular zero-mean Gaussian distribution² with positive definite covariance matrix Σ_X (Σ_Y), complying with the structure introduced in [8], i.e.,

$$\Sigma_X \in \Xi \quad (\Sigma_Y \in \Xi)$$

where

$$\Xi = \left\{ \Sigma \in \mathcal{H}_N^{++} : \Sigma = \begin{pmatrix} \Sigma_1 & \mathbf{0} \\ \mathbf{0} & \sigma^2 \end{pmatrix} \right\}. \quad (1)$$

Under the aforementioned settings, the change detection problem in region \mathcal{A} can be formulated in terms of the following binary hypothesis test:

$$\begin{cases} H_0 : \Sigma_X = \Sigma_Y \\ H_1 : \Sigma_X \neq \Sigma_Y \end{cases} \quad (2)$$

where the null hypothesis H_0 of change absence is tested versus the alternative H_1 . Exploiting the Gaussian assumption together with the covariance structure (1), we can write the joint probability density function (pdf) of \mathbf{R}_X and \mathbf{R}_Y as³

$$f_{\mathbf{R}_X, \mathbf{R}_Y}(\mathbf{R}_X, \mathbf{R}_Y | H_1, \Sigma_{X,1}, \Sigma_{Y,1}, \sigma_{X,1}^2, \sigma_{Y,1}^2) = \frac{1}{\pi^{6K} \det^K(\Sigma_{X,1}) \det^K(\Sigma_{Y,1}) \sigma_{X,1}^{2K} \sigma_{Y,1}^{2K}}$$

¹For example, the technique proposed in [9] can be used to perform the coregistration of the images.

²The same GLRT detector could be obtained under the assumption of complex multivariate elliptical contoured distribution for the observations [10].

³The inverse of a block-diagonal matrix in the class Ξ still belongs to Ξ . This property is used to compute $\text{tr}(\Sigma_X^{-1} \mathbf{S}_X)$ and $\text{tr}(\Sigma_Y^{-1} \mathbf{S}_Y)$.

$$\times \exp \left\{ -\text{tr} \left(\Sigma_{X,1}^{-1} \mathbf{S}_{X,1} + \Sigma_{Y,1}^{-1} \mathbf{S}_{Y,1} \right) - \frac{\widehat{\sigma}_{X,1}^2}{\sigma_{X,1}^2} - \frac{\widehat{\sigma}_{Y,1}^2}{\sigma_{Y,1}^2} \right\} \quad (3)$$

$$f_{\mathbf{R}_X, \mathbf{R}_Y}(\mathbf{R}_X, \mathbf{R}_Y | H_0, \Sigma_{X,1}, \sigma_{X,1}^2) = \frac{1}{\pi^{6K} \det^{2K}(\Sigma_{X,1}) \sigma_{X,1}^{4K}} \times \exp \left\{ -\text{tr} \left[\Sigma_{X,1}^{-1} (\mathbf{S}_{X,1} + \mathbf{S}_{Y,1}) \right] - \frac{\widehat{\sigma}_{X,1}^2 + \widehat{\sigma}_{Y,1}^2}{\sigma_{X,1}^2} \right\} \quad (4)$$

where \mathbf{S}_X and \mathbf{S}_Y are partitioned as

$$\mathbf{S}_X = \begin{bmatrix} \mathbf{S}_{X,1} & \mathbf{S}_{X,2} \\ \mathbf{S}_{X,2}^\dagger & \widehat{\sigma}_{X,1}^2 \end{bmatrix} \quad \mathbf{S}_Y = \begin{bmatrix} \mathbf{S}_{Y,1} & \mathbf{S}_{Y,2} \\ \mathbf{S}_{Y,2}^\dagger & \widehat{\sigma}_{Y,1}^2 \end{bmatrix} \quad (5)$$

and $\widehat{\sigma}_{X,1}^2$ and $\widehat{\sigma}_{Y,1}^2$ are scalars.

In [3], the GLRT has been devised without considering the special structure (1) for Σ_X and Σ_Y . The resulting detector, referred to in the following as unstructured GLRT, is

$$\frac{\det^2(\mathbf{S}_X + \mathbf{S}_Y)}{\det(\mathbf{S}_X) \det(\mathbf{S}_Y)} \frac{H_1}{H_0} \gtrless T_U \quad (6)$$

where T_U is the detection threshold set to ensure a given P_{fa} level. In the next section, we exploit the special covariance structure (1) induced by polarization diversity and derive the structured GLRT.

III. STRUCTURED GLRT DESIGN

This approach is equivalent to replacing the unknown parameters in the likelihood ratio with their maximum likelihood estimates, under each hypothesis [11]. Specifically, the structured GLRT is the decision rule (7), shown at the bottom of the next page, and after substituting the pdfs defined in (3) and (4), we get (8), shown at the bottom of the next page.

Hence, performing the maximizations over the parameters, we can recast (8) in the equivalent form

$$\frac{\det^{2K}(\mathbf{S}_{X,1} + \mathbf{S}_{Y,1})}{\det^K(\mathbf{S}_{X,1}) \det^K(\mathbf{S}_{Y,1})} \frac{\left(\widehat{\sigma}_{X,1}^2 + \widehat{\sigma}_{Y,1}^2 \right)^{2K}}{\left(\widehat{\sigma}_{X,1}^2 \widehat{\sigma}_{Y,1}^2 \right)^K} \frac{H_1}{H_0} \gtrless T_{S,1} \quad (9)$$

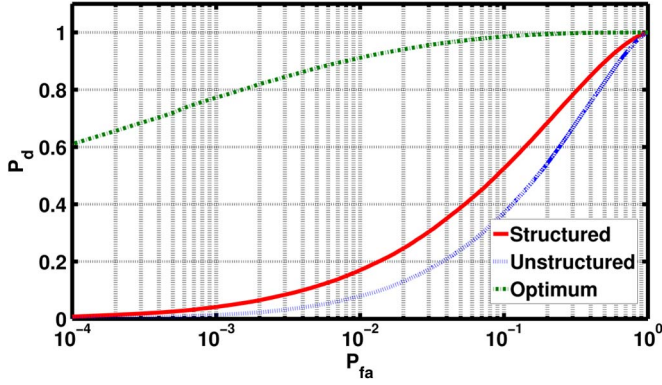
with $T_{S,1}$ being a modified version of $T_{S,0}$. Finally, after a monotonic transformation, we get the following equivalent form of the GLRT:

$$\frac{\det^2(\mathbf{S}_{X,1} + \mathbf{S}_{Y,1})}{\det(\mathbf{S}_{X,1}) \det(\mathbf{S}_{Y,1})} \frac{\left(\widehat{\sigma}_{X,1}^2 + \widehat{\sigma}_{Y,1}^2 \right)^2}{\widehat{\sigma}_{X,1}^2 \widehat{\sigma}_{Y,1}^2} \frac{H_1}{H_0} \gtrless T_S \quad (10)$$

with T_S being the modified detection threshold. It can be proved that (10) ensures the CFAR property with respect to both $\Sigma_{X,1}$ and $\sigma_{X,1}^2$ (see the Appendix which also provides a stochastic representation for the fast simulation of the detector). Otherwise stated, the detection threshold ensuring a given false alarm rate (FAR) can be set independent of the two aforementioned parameters. Before concluding this section, it is important to highlight that a statistically equivalent detector can be obtained by testing the equality of the matrix parameters [sharing the structure (1)] of two statistically independent Wishart distributions [4].

IV. PERFORMANCE ANALYSIS

This section presents the performance analysis for the proposed decision rule for both simulated and real data.

Fig. 2. P_d versus P_{fa} for $W = 3$.

A. Performance Analysis on Simulated Data

This section presents the performance analysis via computer-simulated data of the detectors introduced in Sections II and III. In particular, the standard ROCs are computed for the unstructured and structured GLRTs and compared with the benchmark performance of the optimum Neyman–Pearson detector. In order to set the detection threshold, Monte Carlo simulations are used, assuming $100/P_{fa}$ independent runs. Additionally, 10^5 independent trials are exploited to estimate P_d . As in [3], the theoretical covariance matrices considered to estimate the P_d are

$$\Sigma_X = \begin{pmatrix} 1 & 0.5 & 0 \\ 0.5 & 1 & 0 \\ 0 & 0 & 0.2 \end{pmatrix} \quad \Sigma_Y = 2\Sigma_X$$

while $\Sigma_Y = \Sigma_X$ was considered to estimate the P_{fa} .

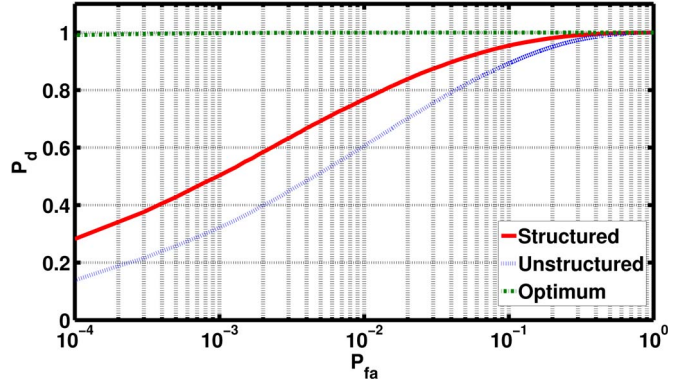
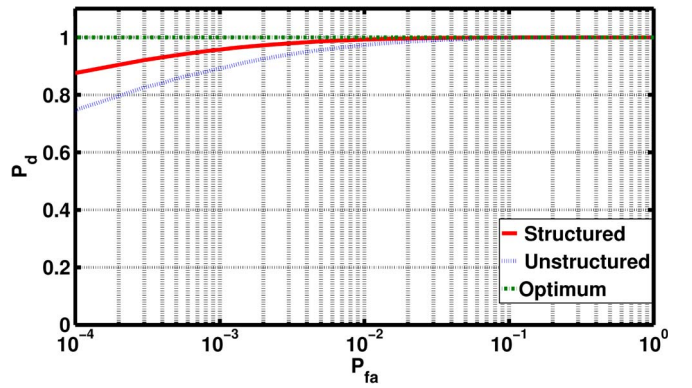
The optimum receiver assumes that the actual covariance matrices are known and can be expressed as

$$\text{tr} \left[(\Sigma_X^{-1} - \Sigma_Y^{-1}) S_Y \right] \stackrel{H_1}{\gtrless} \stackrel{H_0}{T} \quad (11)$$

which, using the special structure of Σ_X and Σ_Y , leads to

$$\text{tr} \left[(\Sigma_{X,1}^{-1} - \Sigma_{Y,1}^{-1}) S_{Y,1} \right] + \left(\frac{1}{\sigma_{X,1}^2} - \frac{1}{\sigma_{Y,1}^2} \right) \hat{\sigma}_{Y,1}^2 \stackrel{H_1}{\gtrless} \stackrel{H_0}{T}. \quad (12)$$

The obtained ROCs for the cases of $W = 3, 5$, and 7 are shown in Figs. 2–4, respectively. In all cases, the structured GLRT outperforms the unstructured one, while the optimum receiver provides the benchmark performance. For example, for the case

Fig. 3. P_d versus P_{fa} for $W = 5$.Fig. 4. P_d versus P_{fa} for $W = 7$.

of $W = 5$ with a P_{fa} of 10^{-4} , the P_d assumes a value of 0.1386 for detector (6), while the values are 0.2822 for detector (10) and 0.9913 for the detector (12). Moreover, note that, for all of the detectors, the P_d improves as W increases for a given P_{fa} . This effect is principally due to the more accurate estimation of the covariance matrices which exploits more homogeneous data.

B. Testing on Real Data

The performance of the method has been evaluated using real X-band data. The data set used is the Coherent Change Detection Challenge data set acquired by the Air Force Research Laboratory [12]. The data contain passes acquired from three polarizations (HH, VV, and HV).

$$\frac{\max_{\Sigma_{X,1}, \Sigma_{Y,1}, \sigma_{X,1}^2, \sigma_{Y,1}^2} f_{\mathbf{R}_X, \mathbf{R}_Y}(\mathbf{R}_X, \mathbf{R}_Y | H_1, \Sigma_{X,1} \Sigma_{Y,1}, \sigma_{X,1}^2, \sigma_{Y,1}^2)}{\max_{\Sigma_{X,1}, \sigma_{X,1}^2} f_{\mathbf{R}_X, \mathbf{R}_Y}(\mathbf{R}_X, \mathbf{R}_Y | H_0, \Sigma_{X,1}, \sigma_{X,1}^2)} \stackrel{H_1}{\gtrless} \stackrel{H_0}{T_{S,0}} \quad (7)$$

$$\frac{\max_{\Sigma_{X,1}, \Sigma_{Y,1}, \sigma_{X,1}^2, \sigma_{Y,1}^2} \left\{ \frac{\exp \left[-\text{tr} \left(\Sigma_{X,1}^{-1} S_{X,1} + \Sigma_{Y,1}^{-1} S_{Y,1} \right) - \frac{\widehat{\sigma}_{X,1}^2}{\sigma_{X,1}^2} - \frac{\widehat{\sigma}_{Y,1}^2}{\sigma_{Y,1}^2} \right]}{\pi^{6K} \det^K(\Sigma_{X,1}) \det^K(\Sigma_{Y,1}) \sigma_{X,1}^{2K} \sigma_{Y,1}^{2K}} \right\}}{\max_{\Sigma_{X,1}, \sigma_{X,1}^2} \left\{ \frac{\exp \left[-\text{tr} \left[\Sigma_{X,1}^{-1} (S_{X,1} + S_{Y,1}) \right] - \frac{\widehat{\sigma}_{X,1}^2 + \widehat{\sigma}_{Y,1}^2}{\sigma_{X,1}^2} \right]}{\pi^{6K} \det^{2K}(\Sigma_{X,1}) \sigma_{X,1}^{4K}} \right\}} \stackrel{H_1}{\gtrless} \stackrel{H_0}{T_{S,0}} \quad (8)$$

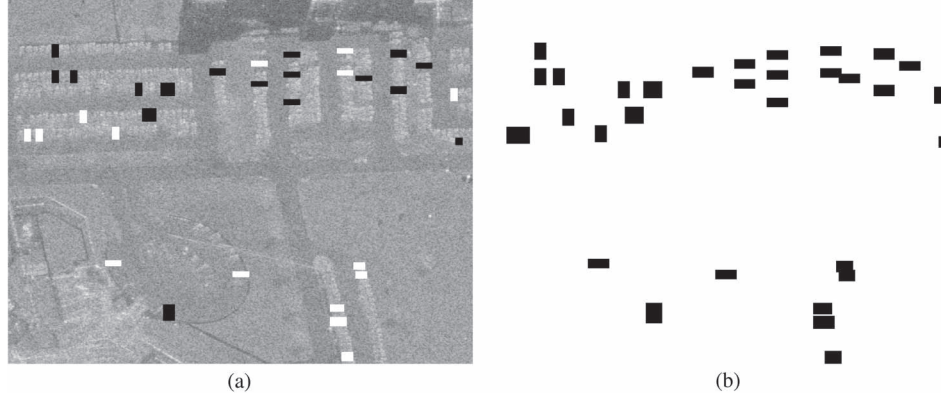


Fig. 5. Ground truth superimposed to the reference image and ground truth with the addition of guard cells. (a) Ground truth. (b) Ground truth with guard cells.

For our analysis, we focus on two acquisitions from the entire data set. Unfortunately, the ground truths of the data were not available (e.g., the actual changes between two different acquisitions). To form an effective ground truth, the best candidate passes were selected, i.e., the acquisition pass named “FP0124” was used as the reference pass, while the acquisition “FP0121” was used as the test pass. The selected area of interest is a subimage of 1000×1000 pixels (i.e., $L = M = 1000$). It comprises several parking lots which are occupied by numerous parked (i.e., stationary) vehicles.

For this particular scenario, the changes between the reference and test images (denoted by \mathbf{X} and \mathbf{Y} , respectively) that occurred during the time interval between the two acquisition passes can be distinguished in the following two cases:

- 1) a vehicle is present in \mathbf{X} but is not present in \mathbf{Y} ; this case is referred to as departure;
- 2) a vehicle is not present in \mathbf{X} but is present in \mathbf{Y} ; this event is referred to as arrival.

Using the cases defined previously and by flickering between the two images (reference and test), a total of 34 changes between \mathbf{X} and \mathbf{Y} are visually identified. The resulting ground truth is shown in Fig. 5(a), wherein the black rectangles represent departures and the white rectangles indicate arrivals.

Although the acquisitions were performed during the same day and the images were registered, the returns from a scatterer can contribute differently to neighbor pixels, e.g., a slightly different aspect angle can produce a different amount of energy spillover. These relative differences in the imaged data can lead to false alarms in the change detection results. For this reason, we consider a guard area around each arrival–departure. This allows the definition of an extended ground truth [see Fig. 5(b)] used in the following to compare the performance of the considered detection algorithms.

In order to assess the performance of the detectors, both the number of detected changes and the change detection maps are presented. For a given decision rule, the corresponding map of changes \mathbf{C} is an $L \times M$ matrix whose (l, m) th entry is the corresponding decision statistic considering the $N \times N$ sample Grammian matrix $\mathbf{S}_{\mathbf{X}_{l,m}}$ ($\mathbf{S}_{\mathbf{Y}_{l,m}}$) evaluated considering a square neighborhood⁴ with size $W \times W$ from the pixel (l, m) of \mathbf{X} (\mathbf{Y}).

⁴We notice that, in order to obtain \mathbf{C} of size $L \times M$, we include a frame of ε pixel width of both reference and test images with $\varepsilon = (W - 1)/2$, in order to be able to compute the statistics on the image borders. By doing so, W must be odd.

TABLE I
NUMBER OF CORRECT DETECTIONS FOR $W = 3, 5$, AND 7

Detector	W		
	3	5	7
Unstructured GLRT (6)	3802	6492	7533
Structured GLRT (10)	4949	6655	7387

The detection map corresponding to \mathbf{C} is then defined as

$$\mathbf{D}(l, m) = \begin{cases} 1 & \text{if } \mathbf{C}(l, m) > T \\ 0 & \text{otherwise} \end{cases} \quad \begin{matrix} l = 1, \dots, L \\ m = 1, \dots, M \end{matrix} \quad (13)$$

where T denotes the detection threshold. In the analysis presented in this section, the thresholds are set to ensure $P_{fa} = 10^{-3}$ in the complement of the extended ground truth area, namely, in the region where no changes occur (there are no true positives). This means that, for each detector, after computing the decision statistics (for each pixel belonging to the complement of the extended ground truth), the threshold has been selected in order that

$$10^{-3} \times \text{total number of available statistics (trials)}$$

are greater than the threshold. This ensures that all of the comparisons refer to the same P_{fa} level, namely, the number of threshold crossings in the complement of the extended ground truth is exactly the same for all of the analyzed detectors. Table I shows the number of correct changes detected using receivers (6) and (10) for the cases with $W = 3$, $W = 5$, and $W = 7$.

From Table I, it is clear that the structured GLRT outperforms the unstructured GLRT for the smaller window sizes ($W = 3$ and 5), whereas the unstructured GLRT outperforms the structured GLRT for the larger window size of $W = 7$ when it is able to detect more changes in the image. This last result can be justified in terms of a covariance model mismatch in the sense that the off-diagonal entries (1,3) and (3,1) of the polarimetric covariance matrix which in the theoretical model have been set to zero might not be exactly zero in reality (even if very close to that value). Additionally, there might be some other deviations from the theoretical model, for instance, due to environmental nonhomogeneities.

Fig. 6(a) and (b) shows the detection maps for detectors (6) and (10) for the case of $W = 3$, respectively. From the detection maps, the higher number of detections achievable with the detector (10) is appreciable.

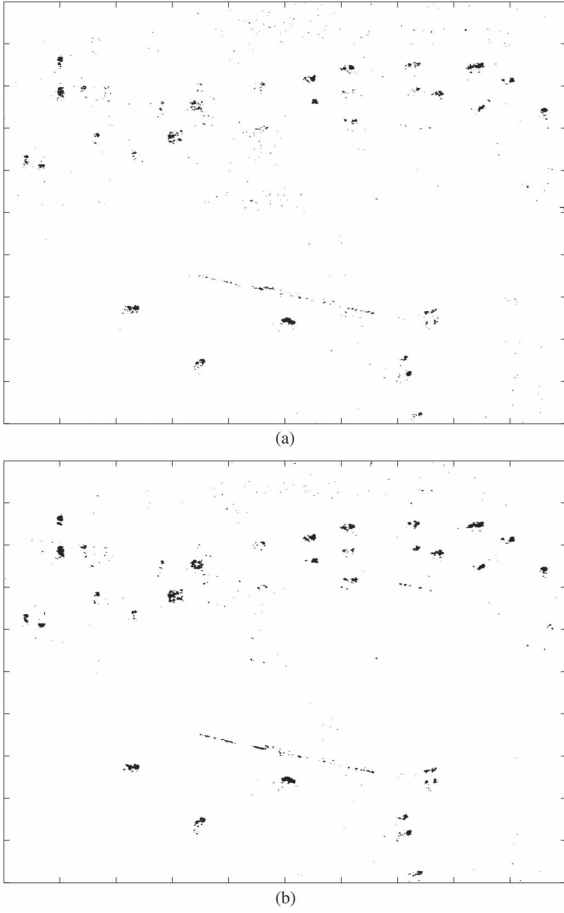


Fig. 6. Detection maps for $W = 3$. (a) Detector (6). (b) Detector (10).

V. CONCLUSION

The block-diagonal structure for the polarimetric covariance matrix has been exploited in this letter to derive a decision rule based on the GLRT criterion. The proposed approach ensures the CFAR property with respect to the unknown polarimetric covariance. The structured GLRT detector has been compared with the unstructured GLRT, with analysis on both simulated and real full-polarimetric SAR data. The performance analysis confirmed that a structured approach can provide increased performance with particular benefits when a small amount of homogeneous data is available. Future work will concentrate on the performance analysis on other data sets, the study of model sensitivity to mismatches, the development of an invariant framework accounting at the maximal invariant design stage of the block-diagonal structure of the polarimetric covariance matrix, and a possible postprocessing using Markov random fields.

APPENDIX

To prove the CFAR property, it is sufficient to observe that, under H_0 ,

- 1) \mathbf{S}_X and \mathbf{S}_Y are identically distributed complex Wishart random matrices with scale parameter K and matrix parameter Σ_X [13];

- 2) $\hat{\sigma}_{X,1}^2$ and $\hat{\sigma}_{Y,1}^2$ admit the following stochastic representation:

$$\hat{\sigma}_{X,1}^2 = \sigma^2 \chi_1, \quad \hat{\sigma}_{Y,1}^2 = \sigma^2 \chi_2 \quad (14)$$

with χ_1 and χ_2 being two complex chi-square random variables with K degrees of freedom.

Moreover, \mathbf{S}_X , \mathbf{S}_Y , χ_1 , and χ_2 are statistically independent. It follows that the left-hand side of (10) can be rewritten as

$$\frac{\det^2 \left[\Sigma_X^{\frac{1}{2}} (\tilde{\mathbf{S}}_{X,1} + \tilde{\mathbf{S}}_{Y,1}) \Sigma_X^{\frac{1}{2}} \right]}{\det \left(\Sigma_X^{\frac{1}{2}} \tilde{\mathbf{S}}_{X,1} \Sigma_X^{\frac{1}{2}} \right) \det \left(\Sigma_X^{\frac{1}{2}} \tilde{\mathbf{S}}_{Y,1} \Sigma_X^{\frac{1}{2}} \right)} \frac{(\chi_1 + \chi_2)^2}{\chi_1 \chi_2} \quad (15)$$

or equivalently as

$$\frac{\det^2 \left(\tilde{\mathbf{S}}_{X,1} + \tilde{\mathbf{S}}_{Y,1} \right)}{\det \left(\tilde{\mathbf{S}}_{X,1} \right) \det \left(\tilde{\mathbf{S}}_{Y,1} \right)} \frac{(\chi_1 + \chi_2)^2}{\chi_1 \chi_2} \quad (16)$$

with $\tilde{\mathbf{S}}_{X,1}$ and $\tilde{\mathbf{S}}_{Y,1}$ being two independent and identically distributed complex Wishart random matrices with scale parameter K and identity matrix parameter.

The stochastic representation in (16) highlights that the decision statistic in (10) can be expressed in terms of random variables whose marginal pdf (and, hence, also their joint pdf due to the statistical independence) is functionally independent of Σ_X . This implies that the CFAR property is achieved.

REFERENCES

- [1] M. Preiss and N. J. S. Stacy, "Coherent Change Detection: Theoretical Description and Experimental Results," Intell., Surveillance Reconnaissance Div., Def. Sci. Technol. Org., Edinburgh, Australia, DSTO-TR-1851, Aug. 2006.
- [2] R. Touzi, A. Lopes, J. Bruniquel, and P. W. Vachon, "Coherence estimation for SAR imagery," *IEEE Trans. Geosci. Remote Sens.*, vol. 37, no. 1, pp. 135–149, Jan. 1999.
- [3] L. M. Novak, "Change detection for multi-polarization, multi-pass SAR," Proc. SPIE Conf.—Algorithms for Synthetic Aperture Radar Imagery XII, Orlando, FL, USA, Mar. 2005, pp. 234–246.
- [4] K. Conradsen, A. A. Nielsen, J. Schou, and H. Skriver, "A test statistic in the complex Wishart distribution and its application to change detection in polarimetric SAR data," *IEEE Trans. Geosci. Remote Sens.*, vol. 41, no. 1, pp. 4–19, Jan. 2003.
- [5] H. Hongtao and B. Yifang, "Unsupervised change detection in multi-temporal SAR images over large urban areas," *IEEE J. Sel. Topics Appl. Earth Obs. Remote Sens.*, vol. 7, no. 8, pp. 3248–3261, Aug. 2014.
- [6] S. Xin, C. A. Deledalle, F. Tupin, and S. Hong, "Change detection and classification of multi-temporal SAR series based on generalized likelihood ratio comparing-and-recognizing," in *Proc. IEEE IGARSS*, Jul. 13–18, 2014, pp. 1433–1436.
- [7] V. Carotenuto, A. De Maio, C. Clemente, and J. J. Soraghan, "Invariant rules for multipolarization SAR change detection," *IEEE Trans. Geosci. Remote Sens.*, vol. 53, no. 6, pp. 3294–3311, Jun. 2015.
- [8] L. M. Novak and M. C. Burl, "Optimal speckle reduction in polarimetric SAR imagery," *IEEE Trans. Aerosp. Electron. Syst.*, vol. 26, no. 2, pp. 293–305, Mar. 1990.
- [9] R. Scheiber and A. Moreira, "Coregistration of interferometric SAR images using spectral diversity," *IEEE Trans. Geosci. Remote Sens.*, vol. 38, no. 5, pp. 2179–2191, Sep. 2000.
- [10] A. De Maio, "Generalized CFAR property and UMP invariance for adaptive signal detection," *IEEE Trans. Signal Process.*, vol. 61, no. 8, pp. 2104–2115, Aug. 2013.
- [11] H. L. Van Trees, *Detection, Estimation, and Modulation Theory*, Part 1. New York, NY, USA: Wiley, 1968.
- [12] S. Scarborough *et al.*, "A challenge problem for SAR change detection and data compression," in *Proc. SPIE*, Apr. 18, 2010, vol. 7699, Algorithms for Synthetic Aperture Radar Imagery XVII, Art. ID. 76990U.
- [13] A. T. James, "Distribution of matrix variates and latent roots derived from normal samples," *Ann. Math. Statist.*, vol. 35, no. 2, pp. 475–501, 1964.